Spectral CT data acquisition with Medipix3.1

2013 JINST 8 P10012

(http://iopscience.iop.org/1748-0221/8/10/P10012)

PUBLISHED BY IOP PUBLISHING FOR SISSA MEDIALAB

RECEIVED: *August 12, 2013*
REVISED: *September 9, 2013*
ACCEPTED: *September 15, 2013*
PUBLISHED: *October 11, 2013*

Spectral CT data acquisition with Medipix3.1

M.F. Walsh,[a,1] S.J. Nik,[b] S. Procz,[c] M. Pichotka,[c] S.T. Bell,[d] C.J. Bateman,[a] R.M.N. Doesburg,[b] N. De Ruiter,[a] A.I. Chernoglazov,[e] R.K. Panta,[a] A.P.H. Butler[a,d,e,f] and P.H. Butler[b,d,f]

[a] *Centre for Bioengineering & Nanomedicine, University of Otago Christchurch, 2 Riccarton Ave, Christchurch, New Zealand*
[b] *Department of Physics and Astronomy, University of Canterbury, Private Bag 4800, Christchurch 8140, New Zealand*
[c] *Freiburger Materialforschungszentrum FMF, Albert-Ludwigs-Universität Freiburg, Freiburg, Germany*
[d] *MARS BioImaging Ltd, 29a Clyde Rd, Christchurch, New Zealand*
[e] *HITLabNZ, University of Canterbury, Private Bag 4800, Christchurch, New Zealand*
[f] *Organisation Européenne pour la Recherche Nucléaire (CERN), Geneva, Switzerland*

E-mail: mike.walsh@otago.ac.nz

ABSTRACT: This paper describes the acquisition of spectral CT images using the Medipix3.1 in spectroscopic mode, in which the chip combines 2×2 pixel clusters to increase the number of energy thresholds and counters from 2 to 8. During preliminary measurements, it was observed that the temperature, DAC and equalisation stability of the Medipix3.1 outperformed the Medipix3.0, while maintaining similar imaging quality. In this paper, the Medipix3.1 chips were assembled in a quad (2×2) layout, with the four ASICs bump-bonded to a silicon semiconductor doped as an np-junction diode. To demonstrate the biological imaging quality that is possible with the Medipix3.1, an image of a mouse injected with gold nano-particle contrast agent was obtained. CT acquisition in spectroscopic mode was enabled and examined by imaging a customised phantom containing multiple contrast agents and biological materials. These acquisitions showed a limitation of imaging performance depending on the counter used. Despite this, identification of multiple materials in the phantom was demonstrated using an in-house material decomposition algorithm. Furthermore, gold nano-particles were separated from biological tissues and bones within the mouse by means of image rendering.

KEYWORDS: Computerized Tomography (CT) and Computed Radiography (CR); Data acquisition concepts

[1] Corresponding author.

doi:10.1088/1748-0221/8/10/P10012

Contents

2013 JINST 8 P10012

1 Introduction

Spectral CT is a developing field of research. One of the key features of spectral CT is to provide material separation of CT images by analysing the energy information of transmitted photons. By utilising K-edges and other characteristic information in the absorption spectra, materials can be identified and quantitatively analysed. Some of the applications of spectral CT include: vascular imaging [1], atherosclerotic plaque identification [2], quantitative soft tissue imaging [3] and separating barium from iodine [4].

To enable spectral CT, an energy-resolving detector is required. One example of these detectors is the Medipix detector. The Medipix family of detectors are a series of hybrid photon counting detectors that use a semiconductor sensor layer to directly convert x-ray photons into an electrical signal (See figure 1). When a photon is detected, an electron-hole pair is created which further ionises a charge cloud of electron-hole pairs. A high voltage bias across the sensor drives this charge cloud to the pixel terminal in the Application Specific Integrated Circuit (ASIC). This induces an electrical signal with a pulse height proportional to the energy deposited by the photon interaction event. Within the Medipix ASIC, the pulse created by the photon detection event is individually analysed. Only photons higher than a preset threshold are recorded by the photon counter. By using multiple thresholds, Medipix detectors can sort photons into user-programmable energy bins. The Medipix3 [5] is the newest generation of Medipix detector. The conventional operation of the chip is in fine pitch mode (FPM) with 256×256 pixels at 55 μm pitch, with each pixel containing two energy counters. When operated in spectroscopic mode, the Medipix3 detectors are capable of inter-pixel communication. This allows for 128×128 pixel clusters at 110 μm pitch, with each cluster combining a 2×2 pixels to provide eight energy counters.

Spectroscopic mode is important for spectral CT in several ways. Firstly, it increases signal quality. In the Medipix detector, a counter records photons with energy ranging from a defined energy threshold to the maximum energy of the x-ray source. Since all eight counters receive and process voltage pulses from the same photon events in spectroscopic mode, the quantum noise across shared energy ranges is identical. Two counters may be subtracted to obtain the photon

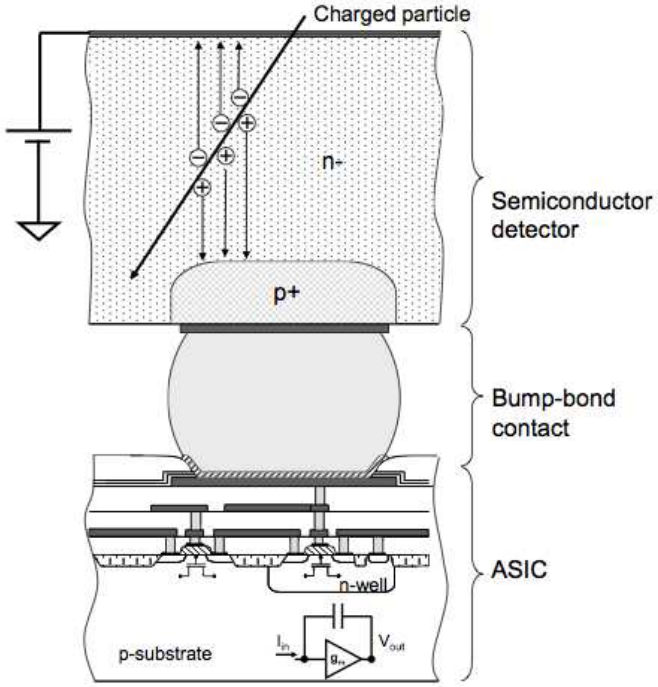

Figure 1. The side view of a Medipix pixel [6] showing the semiconductor sensor layer and the ASIC. Different semiconductor materials can be bump-bonded to the ASIC to act as an x-ray detection layer. When a photon is detected, an electron/hole pair is created. The bias voltage applied across the sensor layer drifts one of the charge clouds to the ASIC end. Within the ASIC, the photon is individually analysed and can be sorted into multiple energy bins. We will show in this work the Medipix3 detector can operate with up to 8 energy bins.

counts from the energy range defined by the two threshold energies, creating an energy bin with only the quantum noise from this energy range. For example, a counter at 25 keV can be subtracted from a counter at 30 keV. This will create an energy bin from 25 keV to 30 keV with quantum noise from photons greater than 30 keV removed. Secondly, being able to acquire eight energy counters in one exposure reduces scan-time, which in effect reduces radiation dose. Thirdly, higher numbers of energy bins have also been shown to be beneficial in material decomposition [7].

In this work, a Medipix3.1 detector was used. The Medipix3.1 is an iteration of the Medipix3 family designed to improve stability, but has the same features for spectroscopic data acquisition. The Medipix3.1 quad (2×2) silicon detector was equalised and operated in spectroscopic mode. This requires the Medipix chips to be bump-bonded at 110 μm pitch, with only one in every four ASIC terminals is connected to the semiconductor sensor layer. Our quad Si-Medipix3.1 chips were bump-bonded at 55 μm pitch during manufacture, with every ASIC terminal bonded to the sensor layer. Partial spectroscopic mode was enabled in software to examine this feature, with the charge-clouds only being collected and compared from a 55×55 μm^2 region, and the charge from the other 3 ASIC terminals discarded.

2013 JINST 8 P10012

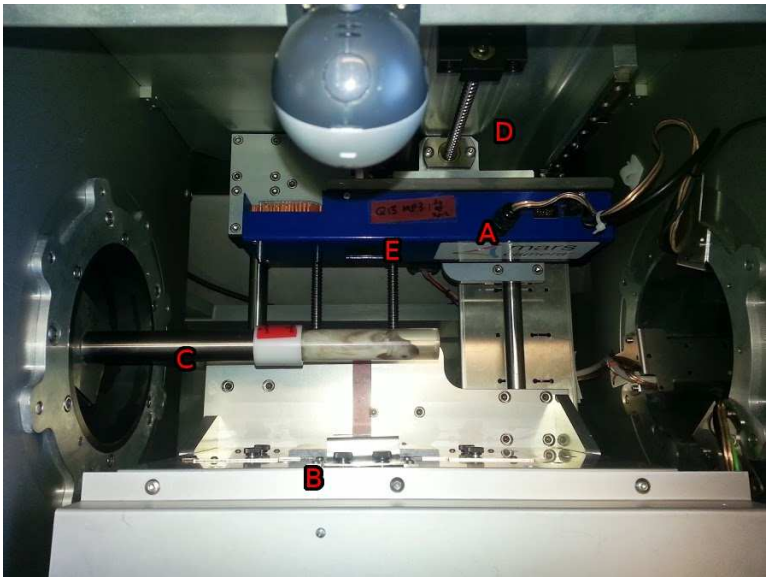

Figure 2. The MARS-CT internal gantry and the MARS camera. A) shows the MARS camera; B) shows the x-ray source with manually controllable collimation; C) shows a customised sample mounted on the retractable sample bed; D) shows the camera translation movement axis; and E) shows the active detection area of the MARS camera.

2 Materials and methods

The Medipix-All-Resolution-System[1] (MARS) research group is a multi-disciplinary team developing spectral CT systems using the Medipix detector. We have built an animal spectral CT scanner to test and validate the Medipix detector technology. The MARS-CT [8] has an internal gantry with up to 370 degrees of rotational movement, motorised sample bed and camera that provide movements to extend the field of view, as well as mechanical motors for adjusting the source to object distance and object to detector distance. The mechanical layout of the camera inside the MARS-CT gantry is shown in figure 2, with labels for identification of its components.

A MARS-CT scanner, comprised of a MARS camera and a micro-focus x-ray source (Source-Ray Inc, Ronkonkoma, NY, U.S.A.), was employed in this work. The Source-Ray SB-80-1K x-ray source [9] has a tungsten anode and intrinsic filtration of 1.8 mm aluminium (equivalent) and the MARS camera consists of a quad Medipix3.1 detector attached to a Peltier cooling device. A custom readout circuit is used to interface the Medipix ASICs within the MARS camera to standard 1000baseT Ethernet. The software system comprises of a custom built *libMars* C library and a python interface, which provides control of the MARS camera through a gigabit ethernet cable. Communication with the x-ray source and motors was enabled through an RS-232 serial interface.

The four Medipix3.1 ASICs were bump-bonded to a single $28\times28\,\mathrm{mm}^2$ silicon sensor doped in an np-junction diode arrangement. A positive high voltage of 100 V was biased across the silicon sensor to create a depletion region. The camera was set in spectroscopic mode, allowing for eight energy counters at 110 μm pitch. Charge summing mode was not enabled in these experi-

[1] http://bioengineeringchristchurch.otago.ac.nz/mars/.

2013 JINST 8 P10012

ments. The energy response of all pixels in each chip was calibrated using the MARS threshold equalisation procedure [10].

To demonstrate the imaging capabilities of the Medipix3.1, two separate spectral CT scans were obtained. A mouse is presented for the first scan, to allow assessment of performance in a biological imaging application. This mouse had gold nano-particle contrast agent injected and bound to its kidney, and was cast in resin. The second scan is of a *spectral phantom* containing several elementary solutions at different concentrations. The spectral phantom contains two concentric rings of seven evenly spaced capillaries. The outer ring of capillaries contain calcium chloride, "iodixanol" iodine complex, "Dimeglumine Gadopentetate" gadolinium complex, contrast agent with gold nano-particles, canola oil (to represent fat), water and air, respectively. The inner ring of capillaries were not filled in this measurement.

To measure the mouse and the spectral phantom, the x-ray tube was set to 50 kVp and 100 μA. A series of 720 projections were acquired over 360 degrees to ensure sufficient data sampling. The mouse was imaged across the kidneys in FPM and spectroscopic mode. In FPM, the mouse was only measured with one counter at 15 keV. Due to the low absorption efficiencies of the silicon sensor layer, the 8 energy thresholds in spectroscopic mode were spread evenly, at intervals of 3 keV, up to only 35 keV. The mouse was imaged at thresholds of 15, 18, 20, 23, 26, 29, 32 and 35 keV in a single acquisition as a proof-of-concept study for spectroscopic mode.

Images were reconstructed by means of the filtered back projection technique using Octopus [11]. Comparisons of image noise at different projection angles can be found in [12]. The 15 keV image in spectroscopic mode was colour-coded using a version of ExposureRender [13], which was modified for better interpolation between voxels, to highlight the different materials in the mouse.

Similarly, for the spectral phantom, eight energy thresholds (15, 17, 19, 21, 23, 25, 27 and 29 keV) were measured in a single exposure using the spectroscopic mode. These energy thresholds were selected arbitrarily low, based on the low energy absorption efficiency of the silicon sensor layer. The K-edges of iodine (33.17 keV), gadolinium (50.24 keV) and gold (80.72 keV) are all outside the range of energy thresholds, so material decomposition of these elements will be limited. Regardless, an in-house material decomposition algorithm was applied to the spectral data and an image with materials allocated to colours was created. In addition, a simple signal-to-noise ratio assessment was performed to evaluate the performance of the individual counters upon image reconstruction using Octopus.

3 Results

3.1 Gold nano-particles in the kidney of a mouse

Figure 3 shows the two CT slices of the mouse at 15 keV in the two different scans. The images in both modes demonstrate the expected decrease in spatial resolution in spectroscopic mode. Since the chips are bump-bonded with a pixel pitch of 55 μm, the reconstructed image in FPM is presented as an illustration of the original spatial resolution. Figure 4 shows a rendered image obtained from the data in spectroscopic mode (corresponding to figure 3b) using the modified ExposureRender. The gold nano-particle contrast agent located in the mouse kidneys was highlighted in orange, while other high density materials such as bones were coloured yellow.

2013 JINST 8 P10012

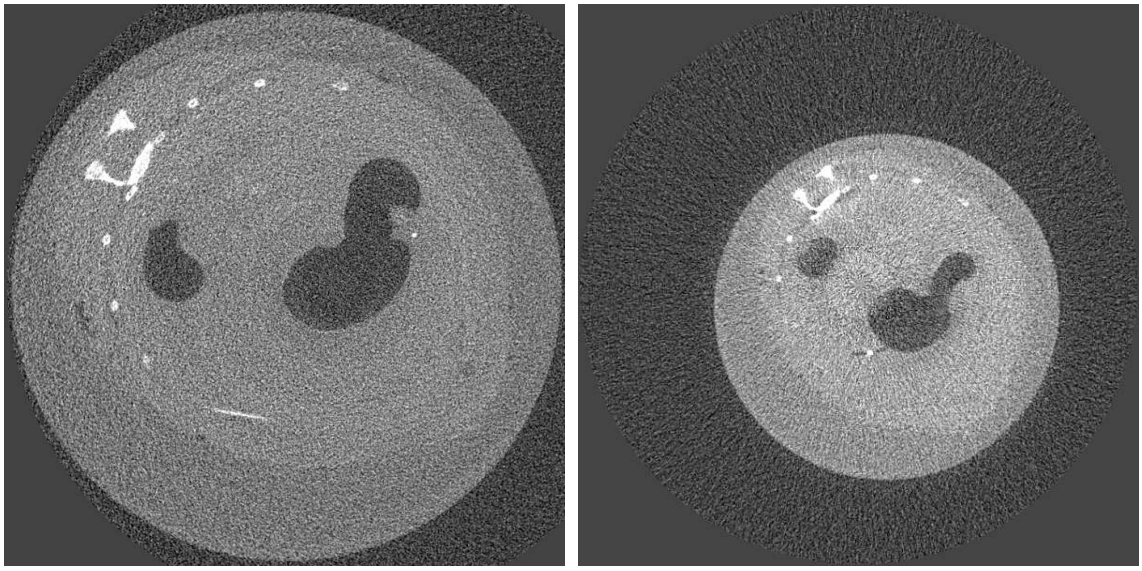

(a) CT slice in FPM at 15 keV

(b) CT slice in spectroscopic mode at 15 keV

Figure 3. CT reconstructions of the mouse with gold nano particles in its liver. Figure (a) has more voxels than figure (b) due to the 55 μ m pixel pitch in (a) as opposed to 110 μm in (b).

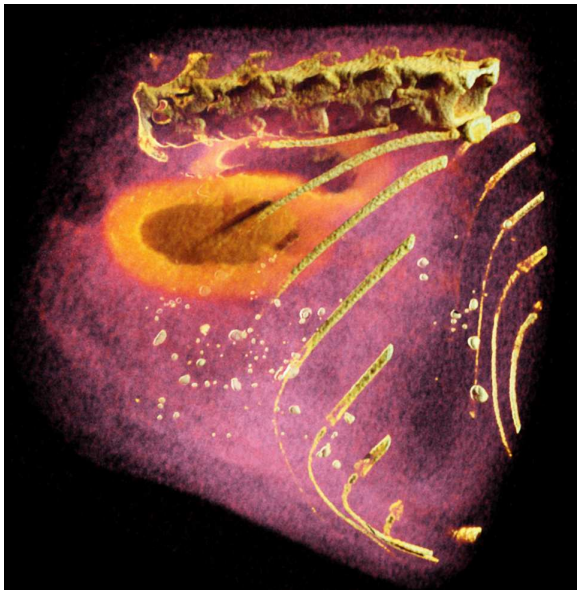

Figure 4. Rendered image of a mouse with gold nano-particles highlighted in orange, as opposed to yellow for other high density materials such as bones.

3.2 Spectral phantom

The reconstructed images of the spectral phantom for the eight energy thresholds are shown in figure 5. All projections were acquired in a single acquisition per rotation angle. The materials in the capillaries are (from the top position and going clockwise) a gadolinium complex (Gd), an iodine complex (I), calcium chloride (Ca), canola oil, water, air and a contrast agent containing

2013 JINST 8 P10012

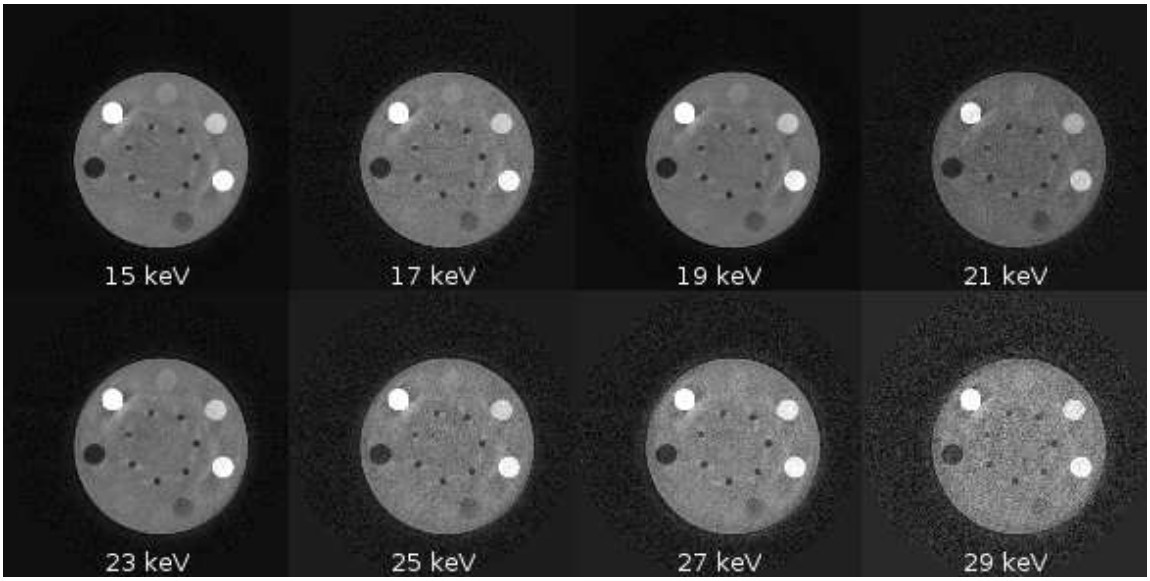

Figure 5. 8 energy CT reconstructions of the spectral phantom, taken with the Medipix3.1. The energy counters were all taken in a single acquisition per rotation step. The capillaries contain (from the top position and going clockwise) a gadolinium complex, an iodine complex, calcium chloride, canola oil, water, air and a contrast agent containing gold nano-particles, respectively. The decomposed image of this phantom is shown in figure 7.

gold nano-particles (Au), respectively. Signal-to-noise ratio (SNR) of the heavier materials, i.e. Au, Ca, I and Gd, were plotted in figure 6a, while the SNR for air, water and oil were plotted in figure 6b. The measured SNR was shown to be counter-dependent (counter 0 or counter 1 in FPM).

Images obtained using counter 1 in FPM, i.e. counters $\{1,3,5,7\}$ or $\{17,21,25,29\}$ keV in spectroscopic mode, have intrinsically lower SNR performance and were plotted using dashed lines to distinguish from the solid lines of counter 0 in FPM (counters $\{0,2,4,6\}$ or $\{15,19,23,27\}$ keV in spectroscopic mode). This difference in SNR across counters was evident for all materials. Note that counters $\{0,2,4,6\}$ and counters $\{1,3,5,7\}$ were labelled on the bottom and top axes, respectively.

Figure 7 shows a material decomposition of the spectroscopic acquisition using an in-house algorithm, colour-highlighting the various materials in the spectral phantom. Calcium was coloured green, iodine was coloured magenta, water was coloured cyan and fat was coloured red. The decomposition could not distinguish some materials from others. The gold nano-particles and Perspex^{TM}were identified as calcium/iodine and fat/water, respectively. For the gold nano-particles, this is because the range of energy thresholds selected was insufficient to measure the k-edge. The Perspex^{TM}is radiographically similar to water and fat. Due to a construction error, the concentration of the gadolinium complex was measured to be too low, and was predominantly water. Therefore, the decomposition algorithm purposefully did not look for this material. The next spectral phantom will be constructed with a higher concentration of the gadolinium complex in its capillary. Furthermore, small speckles of iodine were identified as calcium and vice-versa. This is due to limitations in both the spectral and spatial quality of the measurements taken.

2013 JINST 8 P10012

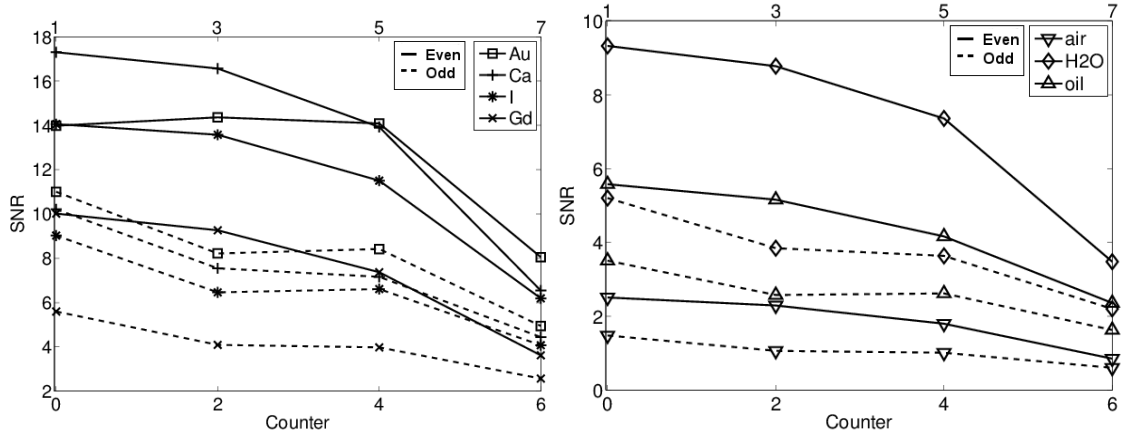

(a) SNR of high-Z materials

(b) SNR of low-Z materials

Figure 6. SNR of the reconstructed images in spectroscopic mode for materials with relatively (a) high and (b) low atomic numbers in the spectral phantom. Note that counters $\{0,2,4,6\}$ (solid lines) and counters $\{1,3,5,7\}$ (dashed lines) were labelled on the bottom and top horizontal axes, respectively. In general, counter 1 in FPM (counters $\{0,2,4,6\}$ or $\{17,21,25,29\}$ keV in spectroscopic mode) shows lower SNR performance than counter 0 in FPM (counters $\{1,3,5,7\}$ or $\{15,19,23,27\}$ keV in spectroscopic mode). This behaviour was evident across all materials.

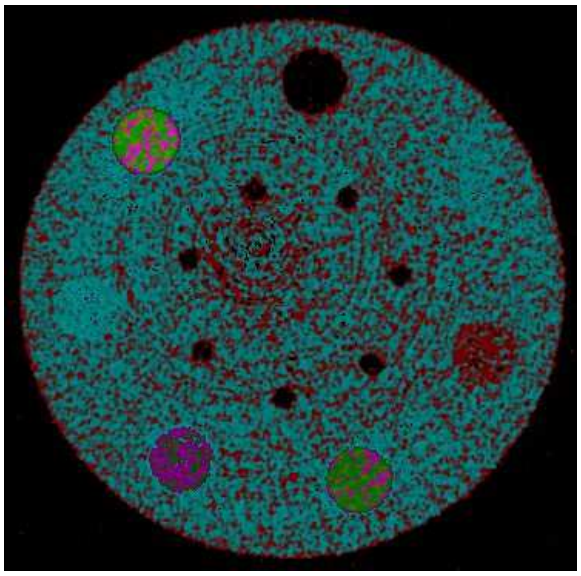

Figure 7. Coloured CT slice of the spectral phantom obtained using an in-house material decomposition algorithm. From the top going clockwise is air, water (cyan), canola oil (red), calcium chloride (green), an iodine complex (magenta), a gadolinium complex and a contrast agent containing gold nano-particles. The gadolinium complex was not included in the decomposition due to a construction error in the spectral phantom. Other limitations of this decomposition include misidentifications of gold nano-particles as calcium/iodine, as well as iodine as calcium and vice-versa. Perspex^{TM}was identified as fat/water given the similarity in attenuation properties of the three materials.

2013 JINST 8 P10012

4 Discussion and conclusions

On the Medipix3.0, the per-pixel configuration for equalisation was not stable with time, with noticeable destabilisation after only two days [10]. The equalisation process ensures that the threshold dispersion in pixel response is minimised for image acquisition by electronically aligning the energy threshold of every pixel. Without equalisation, pixels across a Medipix chip respond unequally when exposed to a constant energy, e.g. a homogeneous x-ray flux. The destabilisation in equalisation can therefore affect both the energy response and the spatial quality of the detector. Similarly, Digital to Analogue Converter (DAC) stability was also an issue in the Medipix3.0 across several key DAC values [14]. Given that the circuitry in each pixel is dependent on the analogue voltages and currents controlled by the DAC values, noise and drift in these parameters can directly affect the detector performance, leading to pixels that vary in count-rate and energy response. These instabilities may be manifested as ring artifacts in the reconstructed images.

The Medipix3.1 was observed to be a more stable chip. Several key DACs, such as the "Cas" DAC, were able to be operated at higher values than allowed in Medipix3.0. For example, the "Cas" DAC on the Medipix3.0 used in figure 8 was only able to achieve 621 mV while measured on the Analogue to Digital Converter (ADC), while the Medipix3.1 could achieve the required 800 mV with no observed instabilities in the Analogue to Digital Converter (ADC) values. The equalisation configurations remained valid for periods over weeks, instead of just two days. In figure 8, a mouse has been scanned with both a Medipix3.0 and a Medipix3.1. The exposure time was 800 ms per projection. The x-ray tube settings were 50 kVp and 400 μA using a W-target source-ray SB-80-1K tube with a 33 μm focal spot. The images are both taken at 15 keV. 720 projection angles were used with a source to detector distance of 205 mm. This comparison shows they have similar levels of contrast quality. The main advantage of the Medipix3.1 is to maintain this level of quality for a longer period of time before recalibration. Although the equalisation configuration used was two weeks old, the reconstructed images in figure 3 and figure 5 show little ring artifacts, demonstrating further the stability improvements of the Medipix3.1 chips for CT imaging.

In FPM, it was found that counter 1 had higher noise than counter 0, due to a limitation in the detector electronics. Given the way the pixels are clustered in spectroscopic mode, counters 0, 2, 4 and 6 (corresponding to counter 0 in FPM) have higher imaging performance compared to counters 1, 3, 5 and 7 (corresponding to counter 1 in FPM). This effect is apparent in figure 6. Furthermore, the quad-Si Medipix3.1 camera used in this work was bump-bonded at 55 μm pixel pitch but was operated in spectroscopic mode. Photons are only counted from a $55\times55\,\mu m^2$ area, which is 4 times smaller than the $110\times110\,\mu m^2$ area expected for spectroscopic mode. The total photon count measured across the chip per exposure was decreased by 75%. Charge sharing is also dependent on pixel size. As the pixel size was not increased by bump-bonding, the chip did not benefit from the possible reduction of charge sharing. This work demonstrates that the Medipix3.1 ASIC is capable of imaging in spectroscopic mode with 55 μm bump-bonding. In particular, separation of materials within a phantom and a mouse was demonstrated. On this basis, it is expected that detectors bump-bonded with 110 μm pitch will have significantly improved imaging properties compared to the detectors evaluated in this paper.

The Medipix3.1 used in this work was bump-bonded to a silicon sensor layer. A silicon sensor layer has a comparatively homogeneous response to a uniform flux, but due to its low atomic

2013 JINST 8 P10012

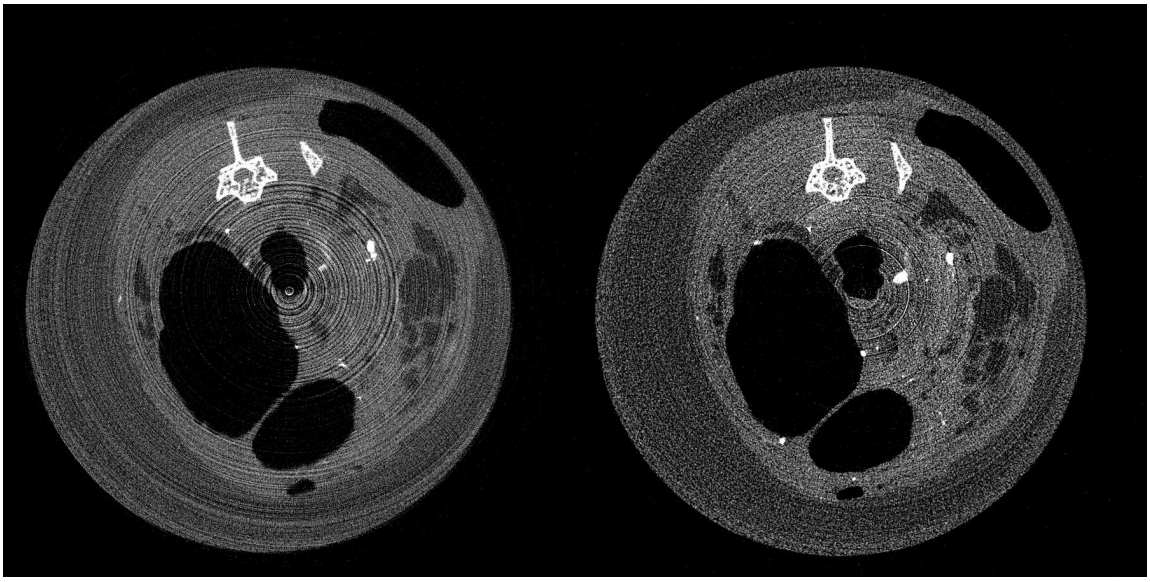

Figure 8. CT reconstructions with a Medipix3.0 and Medipix3.1. The Contrast to Noise Ratio (CNR) between the fat and the air is 3.61 for the Medipix3.0 and 3.79 for the Medipix3.1.

number, has poor photon absorption at energies above 25 keV. Cadmium-telluride [15, 16] or gallium-arsenide [17] are alternatives with higher absorption efficiencies at energies between 30 and 120 keV. These sensor materials are not as readily available as silicon, and were not available with the Medipix3.1 ASIC to the MARS team at the time of these measurements. Consequently, although the image rendering in figure 4 shows visible gold nano-particles in the mouse image taken with the Medipix3.1, this was achieved using the attenuation values rather than from detecting the gold k-edge. The k-edge of gold occurs outside the range of energies that can be measured using a silicon sensor layer. To distinguish gold by its k-edge, a high-Z detector like cadmium-telluride is needed to detect higher energy x-rays. Similarly, in figure 7, the energy thresholds were selected below the K-edges of iodine, gadolinium and gold. It is expected that using a high-Z sensor such as gallium-arsenide or cadmium-telluride would result in improvements in the material decomposition.

The algorithm for decomposition used in figure 7 is a prototype algorithm under development. There were several limitations in allocating materials in this study, where some pixels are allocated incorrect materials from other regions. There are several factors that may have caused this. The energy thresholds were selected at lower energies than required for distinguishing the K-edges of many of the materials of interest. Spatial quality was low, due to insufficient pixel equalisation. This also affects the spectral resolution of the detector, as does charge sharing. Charge summing mode was not used in these measurements. In the Medipix3.0 and Medipix3.1, it is known to suffer from an effect called preferential summing [18, 19], where the lowest threshold pixel has a higher probability of being assigned with the charge in a photon detection event. This made charge summing mode unsuitable for this work. A study on charge summing mode in the Medipix3 detector can be found in [20].

The Medipix3RX is the next version of the Medipix3 detectors. It has a corrected charge summing mode with a counter dedicated to charge arbitration [21]. This corrects the preferential

2013 JINST 8 P10012

summing problem, making charge summing mode useable and allowing for higher spectroscopic performance. It is expected that material decomposition will be improved with measurements using a Medipix3RX chip in charge summing mode.

In conclusion, the Medipix3.1 is an improved chip over the Medipix3.0 for electrical stability. The odd-numbered counters have been shown to be lower quality than the even, due to limitations in the equalisation of the pixel thresholds. With a sensor layer bump-bonded at 55 μm, we have shown that the Medipix3.1 can still acquire high quality spectroscopic CT images. This work has enabled us to integrate spectroscopic mode into the MARS camera. Using this spectroscopic data, we have been able to separate iodine, calcium, fat and water using an in-house material decomposition algorithm. In future, similar measurements will be done in charge summing mode using a Medipix3RX bump-bonded at 110 μm to high-Z sensor materials such as gallium-arsenide or cadmium-telluride.

References

[1] S. Feuerlein et al., *Multienergy photon-counting k-edge imaging: potential for improved luminal depiction in vascular imaging*, *Radiology* **249** (2008) 1010.

[2] D.P. Cormode et al., *Atherosclerotic plaque composition: analysis with multicolor CT and targeted gold nanoparticles*, *Radiology* **256** (2010) 774.

[3] J.P. Ronaldson, *Quantitative soft-tissue imaging by spectral CT with Medipix3*, Ph.D. Thesis, University of Otago, New Zealand (2012) [http://hdl.handle.net/10523/2559].

[4] N.G. Anderson et al., *Spectroscopic (multi-energy) CT distinguishes iodine and barium contrast material in MICE*, *Eur. Radiol.* **20** (2010) 2126.

[5] R. Ballabriga, M. Campbell, E. Heijne, X. Llopart and L. Tlustos, *The Medipix3 Prototype, a Pixel Readout Chip Working in Single Photon Counting Mode With Improved Spectrometric Performance*, *IEEE T. Nucl. Sci.* **54** (2007) 1824.

[6] R. Ballabriga Suñé, *The Design and Implementation in* 0.13μ*m CMOS of an Algorithm Permitting Spectroscopic Imaging with High Spatial Resolution for Hybrid Pixel Detectors*. Ph.D. Thesis, Ramon Llull University, Barcelona, Spain (2009) [CERN-THESIS-2010-055].

[7] X. Wang et al., *Microcomputed tomography with a second generation photon-counting x-ray detector: contrast analysis and material separation*, *SPIE Medical Imaging* **7622** (2010) 76221B.

[8] M.F. Walsh et al., *First CT using medipix3 and the MARS-CT-3 spectral scanner*, 2011 *JINST* **6** C01095.

[9] Source-Ray Inc., *Model SB-80-1K (Doc. M-SB801K-DI, Rev 1) Installation/Operation Manual*, 2002.

[10] M. Walsh, R. Doesburg, J. Mohr, R. Ballabriga, A. Butler and P. Butler, *Improving and characterising the threshold equalisation process for multi-chip medipix3 cameras in single pixel mode*, *IEEE Nuclear Science Symposium and Medical Imaging Conference* (2011) 1718.

[11] M. Dierick, B. Masschaele and L.V. Hoorebeke, *Octopus, a fast and user-friendly tomographic reconstruction package developed in labview®*, *Measurement Science and Technology* (2004) 1366.

[12] N.D. Tang, N. de Ruiter, J.L. Mohr, A.P.H. Butler, P.H. Butler and R. Aamir, *Using algebraic reconstruction in computed tomography*, in proceedings of *27th Conference on Image and Vision Computing New Zealand* (2012), pp. 216–221.

2013 JINST 8 P10012

[13] T. Kroes, F.H. Post and C.P. Botha, *Exposure render: an interactive photo-realistic volume rendering framework*, *PLoS ONE* **7** (2012) e38586.

[14] J.P. Ronaldson, *Characterization of Medipix3 with the MARS readout and software*, 2011 *JINST* **6** C01056.

[15] R. Aamir et al., *Characterization of si and CdTe sensor layers in medipix assemblies using a microfocus x-ray source*, *IEEE Nuclear Science Symposium and Medical Imaging Conference* (2011) 4766.

[16] R. Aamir et al., *Characterization of CdTe x-ray sensor layer on medipix detector chips*, *Mater. Sci. Forum* **700** (2011) 170.

[17] L. Tlustos, M. Campbell, C. Fröjdh, P. Kostamo and S. Nenonen, *Characterisation of an epitaxial GaAs/Medipix2 detector using fluorescence photons*, *Nucl. Instrum. Meth.* **A 591** (2008) 42.

[18] D. Pennicard, R. Ballabriga, X. Llopart, M. Campbell and H. Graafsma, *Simulations of charge summing and threshold dispersion effects in medipix3*, *Nucl. Instrum. Meth.* **636** (2011) 74.

[19] E.N. Gimenez et al., *Study of charge-sharing in MEDIPIX3 using a micro-focused synchrotron beam*, 2011 *JINST* **6** C01031.

[20] R.M.N. Doesburg et al., *Spectrum measurement using Medipix3 in Charge Summing Mode*, 2012 *JINST* **7** C11004.

[21] P.T. Talla, *Investigation of photon counting pixel detectors for X-ray spectroscopy and imaging*, Ph.D. Thesis, Friedrich-Alexander-Universität, Erlangen-Nürnberg, Germany (2011).

2013 JINST 8 P10012